

PIV-based study of a cylindrical roughness element in a hypersonic laminar boundary layer

F. Avallone^{1,2*}, D. Ragni¹, F.F.J. Schrijer¹, F. Scarano¹ and G. Cardone²

¹ AWEF Department, Delft University of Technology, Delft, The Netherlands

² Department of Industrial Engineering, University of Naples “Federico II”, Naples, Italy
*F.Avallone@tudelft.nl

ABSTRACT

In this study, the mean flow organization in the symmetry plane of the recirculation region ahead of a cylindrical roughness element immersed in an incoming laminar boundary layer at Mach number equal to 6.5 is investigated. The flow topology is inspected with planar particle image velocimetry (PIV), InfraRed (IR) Thermography and Schlieren flow visualization. The flow approaching the roughness element forms a main recirculation region ahead of the cylinder leading edge. The reattachment vortex is the responsible of a heat flux local peak in front of the protuberance. Secondary, a more complex system of vortices is observed upstream of the protuberance, which also corresponds to the local maximum of turbulent kinetic energy and wall heat transfer.

1. INTRODUCTION

A critical aspect when designing the thermal protection system (TPS) of a hypersonic re-entry vehicle is the presence of surface protuberances such as junctions or bolts [1], which may cause local over-heating of vehicle surfaces in the hypersonic regime [2, 3].

In practical engineering applications the prediction of the heat flux peak intensity and its location is essential for the design of the TPS. To that end, Estruch-Samper *et al.* [2] investigated the heat transfer in front of 3D short compression ramps (forming different deflection angles with respect to the free stream velocity direction) located on a flat plate and immersed in both a laminar and turbulent boundary layer. The free stream Mach number was varied in the range 8 - 12, while the unit Reynolds number Re_{unit} was kept in the range 3 to $9 \times 10^6 \text{ m}^{-1}$. High-speed Schlieren flow visualizations showed that the region upstream of protuberances features a system of three shock waves. In particular, the presence of a separation shock indicates the occurrence of boundary layer separation with formation of a recirculation region. In the latter case the roughness element was classified as supercritical. They provided a semi-empirical correlation to predict the location of the hot spot region around the protuberance. A similar work was performed by Kumar *et al.* [3], who carried out experiments in a shock tunnel with a free stream Mach number ranging between 6 and 12 with several 3D short compression ramps as protuberances, both installed on a flat plate and a cone. They found a similar shock wave system in presence of a separated region. From their experimental work they established that the length of the upstream separated region on the cone and on the flat plate is approximately 10 or 11 times the roughness height, respectively. Their computations confirmed the presence of a recirculation region with the formation of a horseshoe like vortex that wraps around the roughness element.

From the existing experimental works, any clear experimental evidence of the flow field upstream of the roughness element has been reported yet. Computational studies of this problem have reported rather complex arrangements of vortices upstream of the roughness element, consisting of multiple counter-rotating vortex pairs [4, 5].

In particular, Iyer and Mahesh [4] performed DNS calculations for the experimental conditions of Danehy *et al.* [6] and investigated the influence of a hemispherical roughness element with $k_r/\delta > 1$ with Mach number ranging from 3 to 8. The simulations showed that up to six vortices were observed for Mach numbers from 3 to 5, while a four-vortex system was found at the Mach number equal to 8.23. Similarly, Subbareddy *et al.* [5] performed DNS of the flow around a cylindrical element with $k_r/\delta > 1$ replicating the experiments performed by Wheaton and Schneider [7] and studied the influence of the free stream unit Reynolds number on the transitional flow pattern, confirming the vortex organization reported by Iyer and Mahesh [4].

The present study aims at showing the complex flow structure upstream of a supercritical roughness element ($k_r/\delta = 1.3$). The roughness element is immersed in a laminar boundary layer at free stream Mach number equal to 6.5. Due to the

complexity of performing PIV measurements in the hypersonic regime [8], the present experiment is an unprecedented attempt to characterize the detailed topology of the separated flow region upstream of the roughness element.

2. EXPERIMENTAL SETUP

The experiments are carried out in the hypersonic Ludwig tube (Hypersonic Test Facility Delft, HTFD [9]) at the faculty of Aerospace Engineering of Delft University of Technology. In the present study, the tunnel is operated at a Mach number of 7.5, with a total pressure and total temperature of $p_0 = 28$ bar and $T_0 = 579$ K. For these conditions, the free stream flow velocity is approximately $1030 \text{ m}\cdot\text{s}^{-1}$ with a unit Reynolds number of $Re_{unit} = 14 \times 10^6 \text{ m}^{-1}$. The available run time where the flow exhibits stationary free-stream conditions is approximately 100 ms.

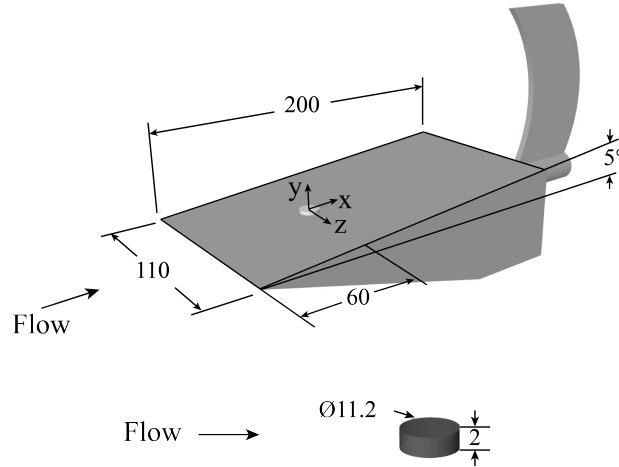


Figure 1 Schematic of the wind tunnel model and roughness element. Dimensions are in mm.

The wind tunnel model is a planar 5° ramp having a length of 200 mm and a width of 110 mm (Fig. 1), it is held from the rear with a sting. The model used for the PIV measurements and the Schlieren visualization is made out of anodized aluminum, while the one used for the heat flux measurements is made out of Makrolon[®].

A cylinder shaped roughness element with a height (k_r) of 2 mm and diameter (D) of 11.2 mm is placed at $x_r = 60$ mm downstream of the leading edge. At the location of the element the undisturbed laminar boundary layer thickness (δ_{99} with respect to the free stream velocity) is approximately 1.5 mm (based on Illingworth-Stewartson transformation for a laminar boundary layer [10]), resulting in k_r/δ equal to 1.3. The momentum thickness (θ) is 0.18 mm and the Reynolds number based on the momentum thickness is $Re_\theta = 2450$.

2.1 INFRARED (IR) THERMOGRAPHY

IR thermography measurements are performed using a CEDIP Titanium 530L IR system. The camera has a mercury cadmium telluride (MCT) quantum detector array of 320×256 pixels and a spectral response of $7.7 - 9.3 \mu\text{m}$. The sensor has an NETD (Noise Equivalent Temperature Difference) of 25 mK. The integration time is set to 400 μs , while the acquisition frame rate is 200 Hz. The camera is equipped with a germanium lens with 25 mm focal length and 2.0 numerical aperture ($f_\#$), which results in a spatial resolution of $2 \text{ px}\cdot\text{mm}^{-1}$.

A coated germanium window with a transmissivity of approximately 0.8 [11] is used to have optical access in the IR wavelength regime. The camera is calibrated using an in-house built blackbody and the presence of the germanium window is included in the calibration process to correct for its reduced transmissivity. The camera is oriented at an angle of approximately 15 degrees with respect to the germanium window to prevent self-reflection. The viewing angle with respect to the model surface is kept less than 50 degrees such that the emissivity can be regarded as constant and independent of the viewing angle [12].

The heat flux is computed by solving a 1D inverse heat transfer problem as described in Avallone *et al.* [13]. According to the error analysis presented in the same study, the heat flux error associated with the inverse data reduction is less than 2%. A full error analysis [14] indicates that the Stanton number measurements are accurate within 8%.

The Stanton number is used to present the measured surface heat flux in its non-dimensional form. It is computed from the surface heat flux using the flow parameters behind the leading edge shock:

$$St = \frac{q_w}{\rho_e c_{pe} U_e (T_w - T_{aw})} \quad (1)$$

where q_w , c_{pe} , T_w , T_{aw} , ρ_e and U_e , respectively represent the wall heat flux, the constant pressure specific heat, the wall temperature, the adiabatic wall temperature and the flow density and speed.

2.2 SCHLIEREN IMAGING

In order to get a qualitative overview of the flow field, a Z-type Schlieren system is used. A high-speed Imager Pro HS 4M (2016 × 2016 pixels, 12 bit, 11 μm/px) camera is operated at a frame rate of 1 kHz with an exposure time of 10 μs. The spatial resolution of the Schlieren images is 13 px·mm⁻¹.

2.2 PLANAR PARTICLE IMAGE VELOCIMETRY

The flow is seeded with Titanium dioxide (TiO₂) particles with a crystal size of 50 nm (Kemira UV-TITAN L830) and a nominal bulk density of $\rho_b = 200 \text{ kg}\cdot\text{m}^{-3}$. The particles form porous agglomerates of approximately 400 nm. The particle relaxation time is $\tau = 2.5 \text{ }\mu\text{s}$ [8, 15].

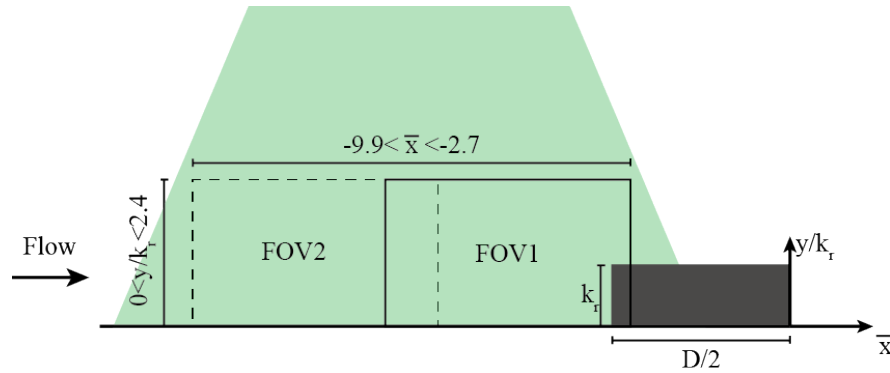


Figure 2 Sketch of the PIV experimental setup and of the investigated FOV: FOV1 continuous line, FOV2 dashed line.

Illumination is provided by a Quantel Twin BSL 200 laser (Nd:YAG, 200 mJ/pulse). The separation time between the two pulses is set to $\Delta t = 0.4 \text{ }\mu\text{s}$. The camera and the laser are both synchronized with the wind tunnel in order to take a measurement at 30 ms after starting the wind tunnel. Due to the short running time of the wind tunnel, only one velocity measurement is obtained for each test.

The particle images are recorded by a PCO Sensicam QE CCD camera (1376 × 1040 pixels, 12 bit, 6.7 μm/px) equipped with Nikon 200 mm focal length Micro objective set at $f_{\#} = 11$. The average image digital resolution is 118 px·mm⁻¹. The area of interest is covered using two fields of view (Fig. 2), thus resulting in a planar measurement domain of 14.4 × 4.8 mm². The two FOVs have a small region of overlap to perform an accurate stitching. The physical domain (FOV1 + FOV2) covers the range $-19.8 \text{ mm} < x - x_r < -5.4 \text{ mm}$ ($-9.9 < \bar{x} = (x - x_r)/k_r < -2.7$) along the streamwise direction and $0 \text{ mm} < y < 4.8 \text{ mm}$ ($0 < y/k_r < 2.4$) along the wall-normal direction.

The illumination and the acquisition systems are synchronized with the wind tunnel control by means of a LaVision programmable timing unit (PTU 9). The DAVIS 7.2 software is used for data acquisition. An in-house built multi-pass algorithm with window deformation and Blackman weighting windows [16] is used to compute the velocity fields. The final interrogation window size is 24 × 32 pixels ($0.20 \times 0.27 \text{ mm}^2$) with an overlap of 75%.

Statistical properties of the flow are inferred from an ensemble of 100 wind tunnel runs for each FOV (and thus also image pairs). The parameters relevant for the PIV setup are reported in Table 1.

The uncertainty in displacement, related to the interrogation area size, and the particle lag effect give the most relevant contribution in the uncertainty of the velocity measurements. The uncertainty in the mean velocity field [17] is assessed at 2% of the free-stream velocity while the uncertainty in the turbulent statistics is assessed at 7% of the free stream velocity. The particle lag effect results in a systematic velocity error (slip velocity V_{slip}), which can be determined from the measured velocity field under steady flow assumption following Ragni *et al.* [18]:

$$V_{slip} = \tau \frac{DV}{Dt} = \tau (\mathbf{V} \cdot \nabla \mathbf{V}) \quad (2)$$

In the formula \mathbf{V} is the velocity vector. It is assessed by using eq. 2 that in the present experiments regions occurred where the particle slip constitutes an appreciable velocity error, not only where the bow shock in front of the roughness is formed. The uncertainty is quantified to be about 9% of the free stream velocity.

Table 1 PIV parameter

Parameter	Value
Measurement plane	$14.4 \times 4.8 \text{ mm}^2$
Digital resolution	$118 \text{ px} \cdot \text{mm}^{-1}$
Laser pulse time separation Δt	$0.4 \mu\text{s}$
Interrogation window	$24 \times 32 \text{ pixels } (0.20 \times 0.27 \text{ mm}^2)$
Interrogation window overlap	75%
Vectors per field	211×123

3. EXPERIMENTAL RESULTS

3.1 MEAN FLOW ORGANIZATION

An overview of the flow field is provided by the Schlieren visualization shown in Fig. 3. In the image four shock waves can be identified: the leading edge shock originating from the nose of the model (the measured shock angle is approximately 10.5° in agreement with the theoretical prediction of 11°), a separation shock, a bow shock formed in front of the roughness element and a compression shock downstream of the protuberance. Since a recirculation region characterizes the region upstream of the protuberance, the roughness can be classified as being supercritical [2, 3].

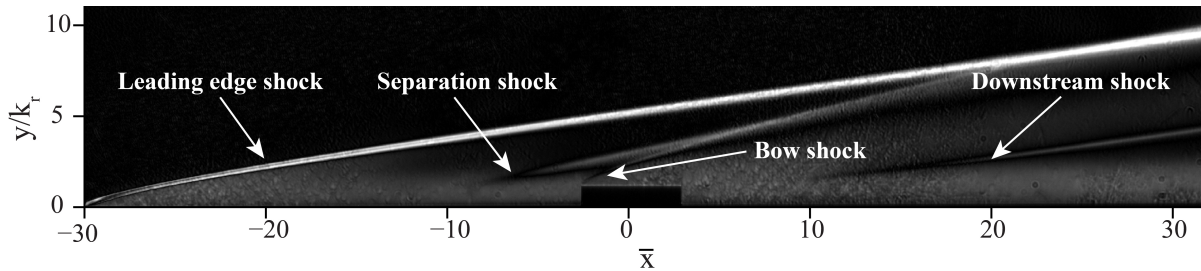


Figure 3 Schlieren flow visualization of the flow field perturbed by the cylindrical roughness element.

On the front edge of the roughness element a bow shock is present which interacts with the separation shock at approximately $\bar{x} = 2.8$. Over the rear edge the flow expands followed by compression due to flow reattachment on the wall. Finally, downstream of the roughness the downstream shock causes the streamlines to become roughly parallel to the wall again [19].

In order to confirm the presence of the separated region upstream of the protuberance the streamwise Stanton number (eq. 1) along the centerline is plotted in Fig. 4. The streamwise evolution of the Stanton number along the model centerline gives a first indication of how strongly the flow is affected by the roughness element. Starting at the leading edge (located at $\bar{x} = -30$) the Stanton number first decreases due to the laminar boundary layer development. At approximately $\bar{x} = -12.9$ the Stanton number decreases more rapidly which can be ascribed to flow separation and a local minimum ($St = 0.22 \times 10^{-3}$) is reached at approximately $\bar{x} = -9.9$. Thereafter the Stanton number increases and a first local maximum ($St = 1.05 \times 10^{-3}$) is detected at approximately at $\bar{x} = -5.8$. After a small decrease, the Stanton number increases and a maximum $St = 1.75 \times 10^{-3}$ is measured at $\bar{x} = -3.9$. After the maximum, the Stanton number shows a steep decrease due to the presence of a small separated region directly upstream of the element. Downstream of the protuberance, a low Stanton number region is measured indicating the presence of a recirculating flow region. At approximately $\bar{x} = 6.7$ a local maximum is detected which then corresponds to flow reattachment downstream of the element. Hereafter the Stanton number further increases again. Starting from approximately $\bar{x} = 17.4$ the Stanton number gradually decreases due to the downstream boundary layer development. At $\bar{x} = 28$ the heat flux increases again, which may be ascribed to transitional features in the wake [20].

In the separated region a complex system of vortices may be present depending on the flow conditions [4, 5, 19]. The Stanton number distribution reported in Fig. 5 indicates the presence of a six-vortex system in agreement with the recent

experimental results reported by Avallone *et al.* [20]. The vortical structures formed by the presence of the protuberance develop downstream as streamwise vortices further inducing high and low heat flux streaks depending on the vortex rotation. Six local maxima corresponding to high heat flux streaks are located in the downwash region between counter-rotating vortex pairs [4]. Moving downstream, traces of secondary structures are visible starting from $\bar{x} = 28$. Corresponding to an increasing Stanton number, the start of the transitional region coincides with a wedge-like spreading of the roughness wake with an estimated angle of approximately 3.1° .

The Stanton number distribution on the wind tunnel model surface shows that the maximum heat transfer rate is observed in proximity of the protuberance as also found by Estruch-Samper *et al.* [2].

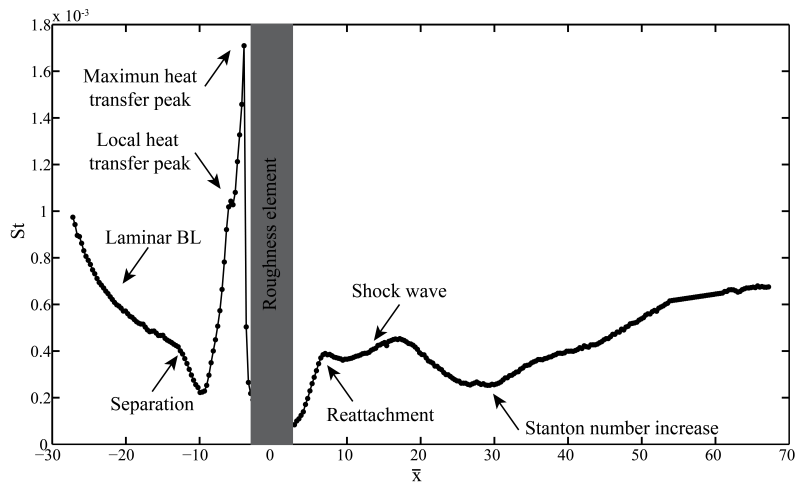


Figure 4 Centerline Stanton number streamwise distribution evaluated by solving a 1D IHTP [13].

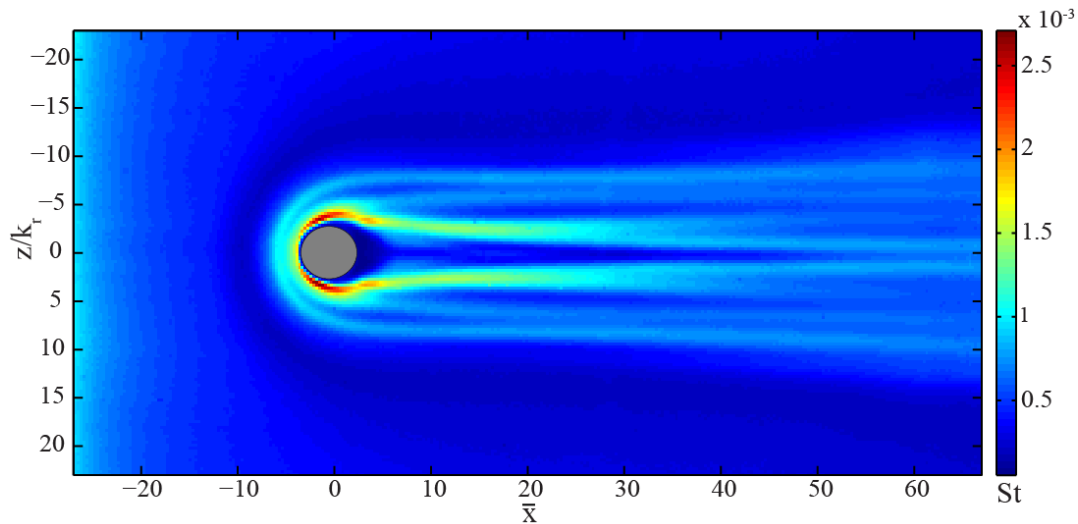


Figure 5 Stanton number distribution on the wind tunnel model surface.

3.2 THE UPSTREAM SEPARATED REGION

The velocity field in the symmetry plane of the recirculation zone in the separated region upstream of the cylindrical protuberance is further studied by means of planar PIV. The mean velocity field is plotted in Fig. 6 where the overall flow topology is visualized through the streamlines. In order to clearly visualize the vortex organization in the separated region a zoom in the range $-6.77 < \bar{x} < -7.58$ and $0.05 < y/k_r < 0.38$ is plotted in Fig. 7.

At the most upstream location of the field of view ($\bar{x} = -9.7$) the flow is already separated. The height of the separated region increases monotonically towards the protuberance edge ($\bar{x} = -2.8$) with a reduced rate in the range $-5.5 < \bar{x} < -3.6$. The mean flow organization shows the presence of six vortices that will be analyzed starting from the most upstream location. At $\bar{x} = -6.6$ a first counter rotating vortex pair is detected (Fig. 7). They are located at approximately the same streamwise location ($\bar{x} = -6.6$) but at two different wall-normal positions. The clockwise rotating vortex is at $y/k_r = 0.16$ while the anti-clockwise rotating one is located at $y/k_r = 0.25$. Their relative position and their orientation do not create any appreciable downwash or upwash on the model surface.

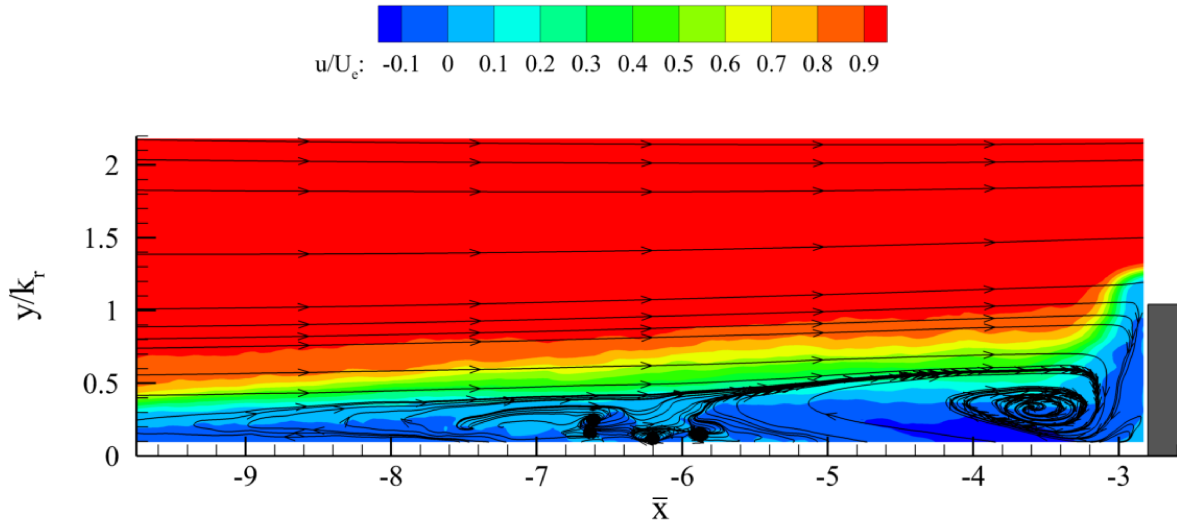


Figure 6 Mean velocity field measured ahead of the cylindrical roughness element.

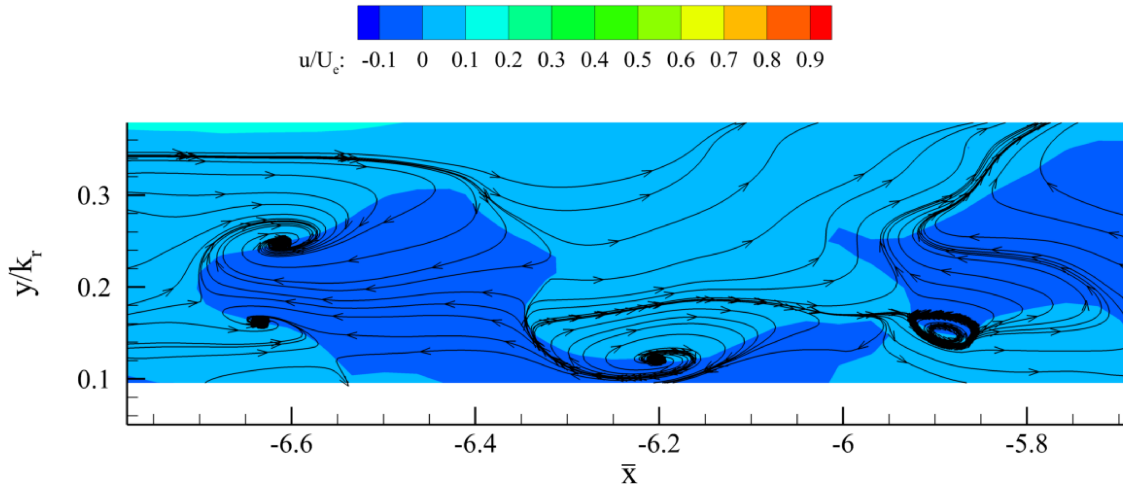


Figure 7 Zoom of the mean velocity field in the range $-6.77 < \bar{x} < 5.68$.

Moving closer to the roughness element, a second pair of vortices is detected with axes at $\bar{x} = -6.2, y/k_r = 0.12$ and $\bar{x} = -5.9, y/k_r = 0.15$, respectively. The stagnation point between the two vortices is located at approximately $\bar{x} = -5.95$. The orientation of the vortices is such that they generate a central downwash in the vicinity of the stagnation point transporting high momentum fluid toward the wall [4]. At approximately $\bar{x} = -5.65$ an upwash motion is visible (Fig. 6), it is generated by the anti-clockwise rotating vortex and by the larger clockwise rotating reattachment vortex present directly ahead of the cylindrical roughness element. The reattachment vortex axis is located at approximately $\bar{x} = -3.6$ and $y/k_r = 0.3$. The main effect of this vortex on the flow is to displace high momentum fluid towards the model surface causing a high heat transfer peak in the centerline Stanton number distribution [4] (cfr. Fig. 4).

Finally, the streamline pattern at $\bar{x} = -3$ and $y/k_r = 0.2$ suggests the presence of a small vortical structure which is under resolved in the present measurements.

The velocity field gives useful information about the shock wave system present in front of the roughness element. Close to the roughness location ($\bar{x} = -2.9$), a strong flow compression followed by a strong downwash close to the edge of the cylindrical protuberance ($\bar{x} = -2.9$ and $y/k_r = 0.2$) is seen from the PIV data (Fig. 6). This compression can be associated to the presence of the bow shock formed in front of the roughness element (Fig. 3).

The current field of view is not large enough to capture the whole separated region and thus the separation point, the latter is therefore estimated by extrapolation. The location of the point where $u/U_e = 0$ is plotted in Fig. 8 and the linear extrapolation of the last 30 measurement points (dashed line in Fig. 8) with the wall represents the separation length. The predicted separation point is estimated at approximately $\bar{x} = -13.3$ resulting in a separation length of approximately $10.5k_r$. The estimated separation length is slightly longer than the one estimated by means of heat flux measurements ($L_{sep} \approx 10k_r$) but in agreement with the one obtained from the linear extrapolation of the separation shock from the Schlieren flow visualizations ($L_{sep} \approx 10.7k_r$) although the differences are minimal. As stated before, the difference between the separation lengths estimated by means of the wall-normal plane measurements and surface measurements are mainly ascribed to the linear extrapolation close to the wall where it is expected that the separation shock curves inward due to the lower velocity.

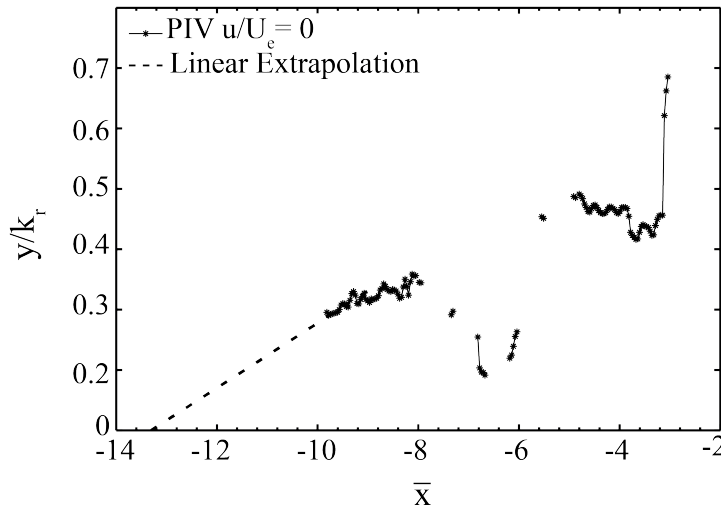


Figure 8 Iso-line of $u/U_e = 0$ extracted from the PIV data (continuous line) and extrapolation until the model surface (dashed line).

In order to relate the heat flux distribution on the model surface with the flow topology in the separated region upstream of the cylinder, a qualitative comparison between the measurements can be done.

As previously stated, at the most upstream location investigated with PIV the flow is already separated. Here, the Stanton number decreases (cfr. Fig. 4). Moving further downstream to the location of the first couple of counter rotating vortices, it is found that they do not cause a traceable feature in the Stanton number. This may be due to the fact that the vortices are relatively weak and they do not generate any downwash or upwash on the model surface (and thus do not generate a local heat transfer maximum or minimum, cfr. Fig. 4). Differently, the second counter rotating vortex pair generates a downwash at approximately $\bar{x} = -5.9$ that may be responsible for the local Stanton number peak measured along the centerline at $\bar{x} = -5.8$ (Fig. 4). Small differences between the two exact locations can be ascribed to the different wind tunnel models, a small uncertainty in the roughness element location and to the availability of the velocity data until $y/k_r = 0.1$. Moreover, the Stanton number distribution on the wind tunnel model surface (Fig. 5) clearly shows that the local maximum region wraps around the cylindrical protuberance, indicating that the vortices do this as well. This footprint suggests that the effect of these counter rotating is limited in the symmetry plane. Furthermore, away from the symmetry plane a Stanton number local minimum is also clearly measured. This may be associated to the upwash generated by the main recirculation vortex present just upstream of the cylindrical protuberance and the anti-clockwise rotating vortex with axis at $\bar{x} = -5.9$.

The location of the main recirculation vortex and the peak in the heat transfer close to the protuberance are also in good agreement. As a matter of fact, in Fig. 6 the streamline pattern suggests that the vortex comes in close proximity with the model surface at approximately $\bar{x} = -3.7$ while a peak in the heat transfer is measured at $\bar{x} = -3.9$. The peak in the heat

transfer close to the protuberance is followed by a rapid decrease of the Stanton number that can be associated to the small separated region formed just ahead of the protuberance.

3.3 VELOCITY FLUCTUATIONS

When a laminar hypersonic boundary layer interacts with a roughness element, possible sources of unsteadiness may be introduced in the flow due to the unsteady vortex system formed in the separated upstream region, shock-induced unsteadiness [3] and shear layer instability [4].

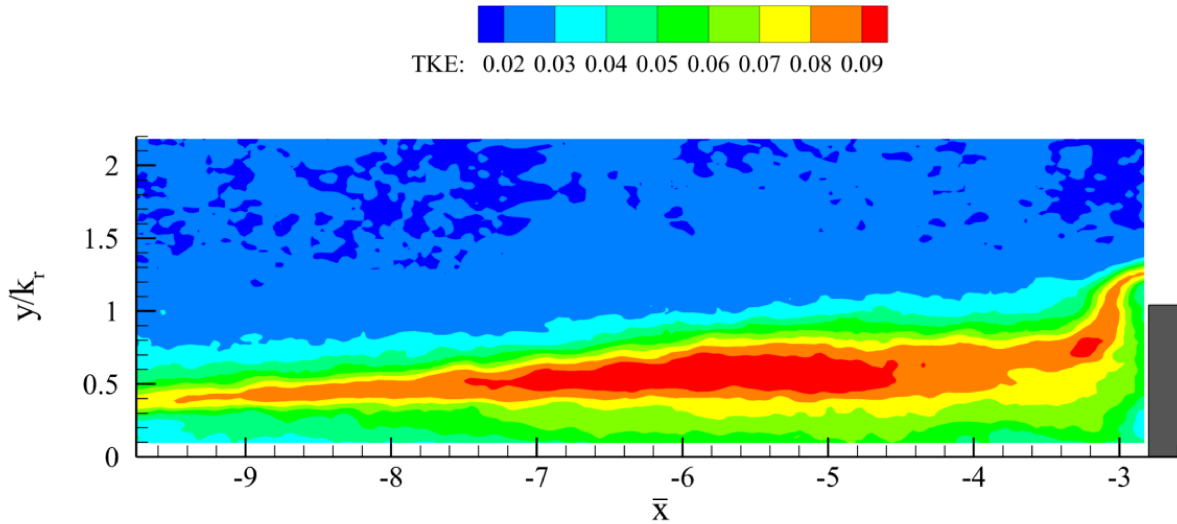


Figure 9 TKE distribution upstream of the roughness element.

The flow unsteadiness upstream of the element is illustrated in Fig. 9 in terms of turbulent kinetic energy $TKE = (\overline{\langle u' \rangle \langle u' \rangle} + \overline{\langle v' \rangle \langle v' \rangle}) / U_\infty^2$ following the description line of Iyer and Mahesh [4]. The TKE distribution shows a region of high unsteadiness localized at $-7.5 < \bar{x} < 4.5$ (the extent of this region is approximately half of the roughness diameter) where a higher concentration of vortices is present. This corresponds to the region where the heat flux exhibits a local increase. The TKE decreases from $\bar{x} = -4.5$ where the reattachment vortex is present suggesting that it is more steady than the more upstream smaller vortices. Moreover, the TKE shows a region of reduced unsteadiness close to the protuberance ($\bar{x} = -2.9$) at almost the same location of the small clockwise rotating vortex. It suggests that here a steady separated region is present. It is confirmed by the smaller Stanton number that is measured close to the roughness element (Fig. 4). In the free stream region the TKE is almost equal to 0.02, which can be attributed to the wind tunnel repeatability and free stream uniformity [9].

Figure 10 shows the wall-normal profile of the TKE in the symmetry plane at five upstream locations. The unsteadiness increases when moving closer to the protuberance; the maximum unsteadiness ($TKE = 0.09$) is detected at approximately $\bar{x} = -6$ (about 1 diameter from the roughness location similarly to [4]) and $y/k_r = 0.6$ indicating that is due to the vortices present in this region. The unsteadiness due to the bow shock formed in front of the roughness element, represented by the last curve in the figure (corresponding to $\bar{x} = -2.9$), is slightly weaker and exhibits a peak ($TKE = 0.08$) at approximately $y/k_r = 1.4$.

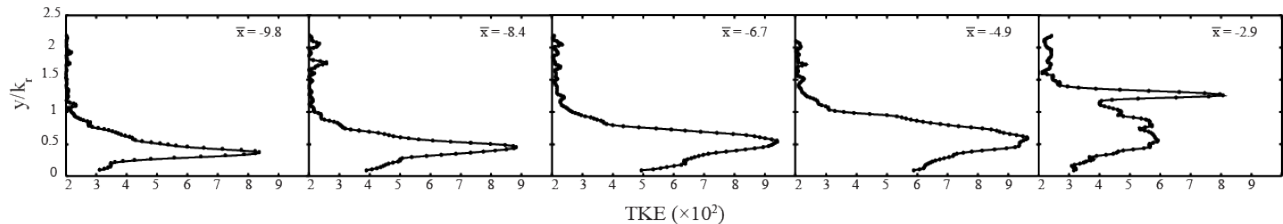


Figure 10 TKE profile at several streamwise locations.

4. CONCLUSIONS

The flow field perturbed by a supercritical roughness element placed in a hypersonic incoming laminar boundary layer is investigated with a particular focus on the upstream separated region.

The mean flow organization is investigated by means of Schlieren flow imaging and heat transfer measurements. The data clearly shows the formation of a separated region upstream through the presence of a separation shock and a local minimum in the streamwise centerline Stanton number distribution. Furthermore, the maximum heat transfer is located around the roughness element. The velocity field measurements confirm the presence of three couple of counter-rotating vortex pair in the recirculation region and their location is quite in agreement with the local Stanton number maxima.

The velocity field turbulent statistics, analyzed through the TKE distribution, show a region of increased unsteadiness at approximately 1 diameter from the protuberance location and it is mainly related to the vortices formed in the recirculation region while the unsteadiness due to the shock wave formed just in front of the roughness is slightly weaker.

ACKNOWLEDGMENTS

This research was supported by Università degli Studi di Napoli Federico II and Compagnia di San Paolo under the "STAR Program 2013"

REFERENCES

- [1] Schneider SP "Effects of Roughness on Hypersonic Boundary-Layer Transition" *Journal of Spacecraft and Rockets* 45 (2008) pp. 193-209
- [2] Estruch-Samper D, MacManus DG, Stollery JL, Lawson NJ and Garry KP "Hypersonic interference heating in the vicinity of surface protuberances" *Experiments in Fluids* 49 (2010) pp. 683-699
- [3] Kumar CS, Singh T and Reddy KPJ "Investigation of the separated region ahead of the three-dimensional protuberances on plates and cones in hypersonic flows with laminar boundary layer" *Physics of Fluids* 26 (2014) 126101 pp. 1-26
- [4] Iyer PS and Mahesh K "High-speed boundary-layer transition induced by a discrete roughness element" *Journal of Fluid Mechanics* 729 (2013) pp. 524-562
- [5] Subbareddy PK, Bartkowicz MD and Candler GV "Direct numerical simulation of high-speed transition due to an isolated roughness element" *Journal of Fluid Mechanics* 748 (2014) pp. 848-878
- [6] Daney PM, Bathel B, Ivey C, Inman JA and Jones SB "NO PLIF study of hypersonic transition over a discrete hemispherical roughness element" AIAA 47th Aerospace Sciences Meeting including The New Horizon Forum and Aerospace Exposition AIAA-2009-0394 (2009)
- [7] Wheaton BM and Schneider SP "Roughness-induced instability in a laminar boundary layer at Mach 6" AIAA 48th Aerospace Sciences Meeting including the New Horizon and Aerospace AIAA 2010-1574 (2010)
- [8] Schrijer, FFJ, Scarano F and van Oudheusden BW "Application of piv in a Mach 7 double-ramp flow" *Experiments in Fluids* 41 (2006) pp. 353-363
- [9] Schrijer, FFJ and Bannink WJ "Description and flow assessment of the Delft hypersonic Ludwig tube" *Journal of Spacecraft and Rockets* 47 (2010) pp. 125-133
- [10] Weigand B, "Analytical Methods for Heat Transfer and Fluid Flow Problems" Springer -Verlag Berlin Heidelberg (2005) Chap. 6.
- [11] Schrijer FFJ "Investigation of Görtler vortices in a hypersonic double compression ramp flow by means of infrared thermography," *Quantitative Infrared Thermography Journal* 7 (2010) pp. 2012-215
- [12] Cardone G, Ianiro A, dello Ioio G and Passaro A "Temperature maps measurements on 3D surfaces with infrared thermography" *Experiments in Fluids* 52 (2012) pp. 375-385
- [13] Avallone F, Greco CS and Ekelschot D "Image resection and heat transfer measurements in hypersonic flows" *Quantitative InfraRed Thermography Journal* 10 (2013) pp. 188-206
- [14] Moffat RJ "Describing the uncertainties in experimental results" *Experimental Thermal and Fluid Science* 1 (1988) pp. 3-17
- [15] Ragni D, Schrijer F, van Oudheusden BW and Scarano, F "Particle tracer response across shocks measured by PIV" *Experiments in Fluids* 50 (2011) pp. 53-64

- [16] Astarita T and Cardone G “Analysis of interpolation schemes for image deformation methods in PIV” *Experiments in Fluids* 38 (2005) pp. 233-243
- [17] Avallone F, Ye Q, Schrijer, FFJ, Scarano F and Cardone G “Tomographic PIV investigation of roughness induced transition in a hypersonic boundary layer” *Experiments in Fluids* 55 (2014) 1852 pp. 1-12, 2014
- [18] Ragni D, Ashock A, van Oudheusden BW and Scarano F “Surface pressure and aerodynamic loads determination of a transonic airfoil based on particle image velocimetry” *Measurements Science and Technology* 20 (2009) 074005 pp. 1-14
- [19] Marxen O, Iaccarino G and Shaqfeh ESG “Disturbance evolution in a Mach 4.8 boundary layer with two-dimensional roughness-induced separation and shock” *Journal of Fluid Mechanics* 648 (2010) pp. 435-469.
- [20] Avallone F, Schrijer FFJ and Cardone G “IR thermography investigation on induced transition by isolated roughness elements in high-speed flows” 12th International Conference on Quantitative InfraRed Thermography QIRT-2014-143 (2014)